Friction **11**(11): 2107–2131 (2023)
https://doi.org/10.1007/s40544-022-0734-2
ISSN 2223-7690
CN 10-1237/TH
RESEARCH ARTICLE

Prediction model of volume average diameter and analysis of atomization characteristics in electrostatic atomization minimum quantity lubrication

Dongzhou JIA[1,2], **Changhe LI**[1,*], **Jiahao LIU**[2], **Yanbin ZHANG**[3,*], **Min YANG**[1], **Teng GAO**[1], **Zafar SAID**[4], **Shubham SHARMA**[5]

[1] *School of Mechanical & Automotive Engineering, Qingdao University of Technology, Qingdao 266520, China*

[2] *College of Mechanical Engineering and Automation, Liaoning University of Technology, Jinzhou 121001, China*

[3] *State Key Laboratory of Ultra-precision Machining Technology, Department of Industrial and Systems Engineering, The Hong Kong Polytechnic University, Hong Kong 999077, China*

[4] *College of Engineering, University of Sharjah, Sharjah 27272, United Arab Emirates*

[5] *Mechanical Engineering Department, University Center for Research and Development, Chandigarh University, Mohali, Punjab 144603, India*

Received: 16 July 2021 / Revised: 05 November 2021 / Accepted: 20 December 2022

Abstract: Minimum quantity lubrication (MQL) is a relatively efficient and clean alternative to flooding workpiece machining. Electrostatic atomization has the merits of small droplet diameter, high uniformity of droplet size, and strong coating, hence its superiority to pneumatic atomization. However, as the current research hotspot, the influence of jet parameters and electrical parameters on the average diameter of droplets is not clear. First, by observing the shape of the liquid film at the nozzle outlet, the influence law of air pressure and voltage on liquid film thickness (h) and transverse and longitudinal fluctuations are determined. Then, the mathematical model of charged droplet volume average diameter (VAD) is constructed based on three dimensions of the liquid film, namely its thickness, transverse wavelength (λ_h), and longitudinal wavelength (λ_z). The model results under different working conditions are obtained by numerical simulation. Comparisons of the model results with the experimental VAD of the droplet confirm the error of the mathematical model to be less than 10%. The droplet diameter distribution span value Rosin–Rammler distribution span (R.S) and percentage concentrations of PM10 (particle size of less than 10 μm)/PM2.5 (particle size of less than 2.5 μm) under different working conditions are further analyzed. The results show that electrostatic atomization not only reduces the diameter distribution span of atomized droplets but also significantly inhibits the formation of PM10 and PM2.5 fine-suspension droplets. When the air pressure is 0.3 MPa, and the voltage is 40 kV, the percentage concentrations of PM10 and PM2.5 can be reduced by 80.72% and 92.05%, respectively, compared with that under the pure pneumatic atomization condition at 0.3 MPa.

Keywords: minimum quantity lubrication (MQL); electrostatic atomization; volume average diameter (VAD); atomization characteristics

1 Introduction

Metal working fluids (MWFs) play an important role in the field of cutting processing, but their base fluid and additives usually contain a large amount of non-renewable mineral oil and harmful substances, such as nitrite, sulfur compounds, chlorinated compounds, and alkanolamine borates, which are

* Corresponding authors: Changhe LI, E-mail: sy_lichanghe@163.com; Yanbin ZHANG, E-mail: zhangyanbin1_qdlg@163.com

Nomenclature

a	Acceleration of the liquid at the nozzle outlet (m/s^2)
C_{Cr}	Limit charge mass ratio (C/kg)
C_D	Drag coefficient
C_z	Real charge mass ratio (mC/kg)
d	Relative distance between electrodes (m)
E_d	Electric field intensity between electrodes (V/m)
E_s	Electric field intensity of r_s point (V/m)
EMQL	Electrostatic atomization minimum quantity lubrication
F_e	Electrostatic field force (N)
F_g	Gas drag force (N)
F_σ	Surface tension (N)
h	Liquid film thickness (m)
k	Surface wave number
L	Length of the annular liquid film (m)
L'	Equivalent length of the annular liquid film (m)
m_l	Mass of the liquid film at the nozzle outlet (kg)
m_l'	Instantaneous mass flow (kg/s)
MQL	Minimum quantity lubrication
MWFs	Metal working fluids
P_e	Electrostatic expansion force (N)
P_s	Static pressure (N)
Q_{Cr}	Limit charge of droplets (C)
Q_d	Total electricity (C)
Q_z	Charge of the liquid film (C)
r_g	Radius of the gas core (m)
r_s	Distance from the calculation point to the center of the sphere (m)
r_0	Radius of the nozzle outlet (m)
R'	Equal-volume spherical diameter of annular liquid film (m)
S_l	Windward area of the annular liquid film (m^2)
S_n	Area directly opposite the two poles (m^2)
U	Nozzle voltage (V)
U_d	Droplet surface potential (V)
v_g	Initial velocity of gas at the nozzle outlet (m/s)
v_l	Liquid phase velocity (m/s)
v_r	Relative velocity of gas and liquid in the nozzle (m/s)
V_l	Volume of the annular liquid film (m^3)
VAD	Volume average diameter of droplet (m)
W_e	Electrostatic energy stored by the droplet (J)
α	Void fraction
ε_r	Relative permittivity of air
ε_0	Dielectric constant of vacuum (C/V·m)
λ_h	Transverse wavelength (m)
λ_z	Longitudinal wavelength (m)
ρ_g	Gas phase density (kg/m^3)
ρ_l	Liquid phase density (kg/m^3)
σ	Liquid surface tension (N/m)
σ^*	Effective surface tension of charged liquid (N/m)
ω	Surface wave growth rate
ω_{max}	Maximum growth rate
ΔW_s	Surface energy variation of the droplet (J)
$\Delta\sigma$	Surface tension reduction (mN/m)

difficult to biodegrade [1–3]. Furthermore, MWFs pose a great threat to the natural environment and the health of operators unless they are post-treated in an environment-friendly manner, but the cost is high. Obviously, MWFs cannot meet the growing demand for low-consumption and efficient clean processing [4–6]. As an extreme green manufacturing method, dry cutting completely abandons the use of MWFs. Although this process can fundamentally solve the negative impact of MWFs, it also leads to the serious shortage of heat exchange capacity. This approach is not suitable for the working conditions of difficult-to-process materials or high-energy-density output [7–9].

Consequently, scholars have proposed the minimum quantity lubrication (MQL) based on the objective reality of flooding and dry cutting. After more than 10 years of exploratory research, MQL has been proven to be a relatively efficient and clean alternative to MWFs [10, 11] given its unique mode of reducing consumption at the supply side. In MQL, compressed air (0.4–0.65 MPa) is used to atomize a small amount of lubricant (10–100 mL/h) either inside or outside the nozzle to form a group of droplets, which are sprayed to the cutting area under the action of air flow field to realize cooling and lubrication [12–14]. As the specific surface area of the lubricant increases

significantly after atomization, its spreading and wetting performance are both improved. Using 5% MWF can achieve an even better processing effect compared with flooding. Knowing how to improve the atomization performance of MQL in terms of droplet size and size distribution as a means of improving the cooling and lubrication ability has become a hot issue among scholars [15–17].

In the past, scholars focused on the commonly used pneumatic atomization mode and performed theoretical analysis and experimental research on atomization performance in this mode. They determined the breaking behavior of liquid films at nozzle outlets under the pull of high-pressure gas as the origin, and thus regarded as the most important consideration. Inamura et al. [18], Brend et al. [19], and Shanmugadas et al. [20] used a high-speed camera to capture the shape and thickness of the liquid film at the outlet of a pneumatic atomizer and the process of the ligament formed by the liquid film under unstable action. They also analyzed the main fluctuation types and dynamic evolution process of the liquid film in the change process of the liquid film. Chaussonnet et al. [21] and Qin et al. [22] built an atomization phenomenological model under the pneumatic atomization condition by considering the law of liquid film fluctuation and liquid film thickness (h) (m), and they predicted the average diameter of the droplets' primary atomization by the pneumatic nozzle. Schillaci et al. [23], Déjean et al. [24], and Lilan et al. [25] adopted the numerical simulation method to analyze and determine different jet parameters, which established as having a significant impact on the fluctuation and evolution of liquid films. They obtained the complete breaking system diagram of the liquid film, determined the internal relationship between the liquid line shape of the liquid film and the main fluctuations of the Kelvin–Helmholtz (K–H) and Rayleigh–Taylor (R–T) waves, and established the prediction model of the average diameter of droplets. Pillai et al. [26] and Zhang et al. [27] analyzed the influence of gas–liquid flow on liquid phase fluctuation based on the principle of liquid instability and discovered the continuous decrease in atomization cone angle with the increase in the gas–liquid momentum ratio. They determined the average diameter and droplet distribution characteristics of droplets by calculating the Weber number and gas–liquid momentum ratio. Dafsari et al. [28] and Bravo et al. [29] show that the smaller the liquid viscosity is, the easier the annular liquid film is to break (0.53–30.25 mm^2/s). Furthermore, although the average diameter of droplets is small, the distribution range of the droplet size is wide.

Gupta et al. [30], Lv et al. [31], and Krolczyk et al. [32] found that increasing the atomization gas pressure could effectively improve the atomization performance and microdroplet transport energy, but negative effects occur at the same time. In the liquid atomization and breaking process, the energy exchange behavior was violent between gas and liquid. The atomization was accompanied by the generation of a large number of fine-oil mist particles, which could easily fly and disperse during movement. Furthermore, the droplet produced by atomization contained a certain amount of PM10 (particle size of less than 10 μm) and PM2.5 (particle size of less than 2.5 μm) particulate matters. The settling time of the PM10 particles was 8.2 s, whereas that of PM2.5 exceeded 1.5 h. Suspended particles in air exceeding a certain concentration will seriously endanger the respiratory system. Fine particles are deposited in the respiratory tract, alveoli, bronchus, and other organs, possibly causing allergy, pneumonia, irritant reaction, asthma, and emphysema or even induce cancer (e.g., laryngeal cancer). In general, vegetable oil is harmless to the health of operators (except for poisonous vegetable oils, such as *Jatropha curcas* oil). However, when operators are exposed to inhalable oil mist particles for a long time in high intensity, a series of respiratory diseases will be caused due to that the human respiratory system cannot load such a large amount of oil mist particles [33, 34]. An analysis of Refs. [35, 36] indicates an irreconcilable contradiction between the improvement of atomization performance and the reduction of environmental impact of the aforementioned methods.

In 2015, Li et al. [37] proposed the electrostatic atomization minimum quantity lubrication (EMQL) grinding technology. Subsequently, Mishra et al. [38] reviewed the development of MQL and determined EMQL to be a green, efficient, and sustainable cooling and lubrication processing method, indicating its broad research and application prospects. Jia et al. [39, 40] and Xu et al. [41] revealed that electrostatic atomization could effectively reduce the average

diameter of atomized droplets and the distribution span of droplet particle size. Moreover, the controllable performance of droplet transport could be enhanced by a certain charge on the droplet surface. Lv et al. [42, 43] conducted experiments on the atomization characteristics of EMQL and obtained similar results apart from a variety of cutting experiments. Their results showed that electrostatic atomization could effectively reduce the temperature and interface friction coefficient in the cutting area, prolong the service life of the tool, and improve the surface quality of the workpiece. Shah et al. [44] proved the improved atomization and tribological properties of a lubricant by charging via friction and wear experiments and 5–15 press hardened steel turning experiments. Su et al. [45] built an EMQL heat transfer performance measurement device and studied the influence of pole spacing, medium flow, and voltage on heat transfer performance. Their results showed that increasing the voltage or selecting a medium flow and reducing the pole spacing could improve the critical heat flux. De Bartolomeis et al. [46] reported the results of a series of cutting experiments on nickel-based alloy 718 under EMQL conditions in the 5th CIRP Conference on Surface Integrity (CSI). They shared that EMQL will likely be a highly competitive method for cutting difficult-to-machine materials in the aerospace field in the future. In Ref. [46], the liquid breaking process includes the violent energy exchange between gas and liquid, which involves a variety of force interactions. Furthermore, the nozzle structure, external environment, liquid physical properties, and other factors have a direct impact on liquid atomization. Introducing the electrostatic field will likely result in an extremely complex liquid breaking mechanism in EMQL.

Knowledge of continuous phase liquid breaking process in EMQL is important in understanding the influence of jet parameters on atomization quality. However, at present, the EMQL process is still in the confirmatory experimental stage of processing effect. The research on the breaking mechanism of the charging liquid of EMQL is relatively scarce. Furthermore, the atomization quality evaluation system for the particle size and size distribution of EMQL is not perfect. Thus, in this study, the fluctuation and evolution law of the liquid film at the outlet of an internal mixing two-phase flow nozzle are studied, and the influence law of the electric field on liquid film fluctuation and its causes are analyzed. First, the three-dimensional geometric quantities of the transverse wavelength (λ_h) (m), longitudinal wavelength (λ_z) (m), and annular film thickness of the liquid film at the outlet of the nozzle are considered, and the mathematical model of the volume average diameter (VAD) of droplets in the annular breaking process of the liquid film at the outlet of the two-phase flow electrostatic nozzle is constructed. Then, the reliability of the mathematical model is verified by a laser particle size measurement experiment. The effects of electrostatic field on the droplet size distribution span and the percentage concentration of fine droplets (i.e., PM10 and PM2.5) during atomization are analyzed. Finally, the atomization mechanism of the breaking process of the liquid film in the microlubrication atomization system under the coupling action of air flow field and electrostatic field is revealed.

2 Analysis of instability fluctuation of the annular liquid film

The internal mixing two-phase flow nozzle has been widely used in the field of MQL because of its advantages of low atomization pressure, low manufacturing and maintenance cost, and low influence of liquid viscosity. The EMQL system used in this study is shown in Fig. 1(a). The nozzle is an internal mixing two-phase flow copper nozzle, and its internal surface roughness (R_a) is 0.23 μm. A pole of the high-voltage direct current (DC) power supply is connected to the contact electrostatic nozzle (self-made type), whereas the other pole is connected to the workpiece for processing. Non-uniform electric field is formed between the nozzle and workpiece. The compressed gas and microlubricant required by the electrostatic nozzle are provided by the MQL system. Energy exchange occurs between the compressed gas and microlubricant in the mixing chamber of the nozzle, and the microlubricant is charged through contact with the nozzle. The specific structure of the electrostatic nozzle is shown in

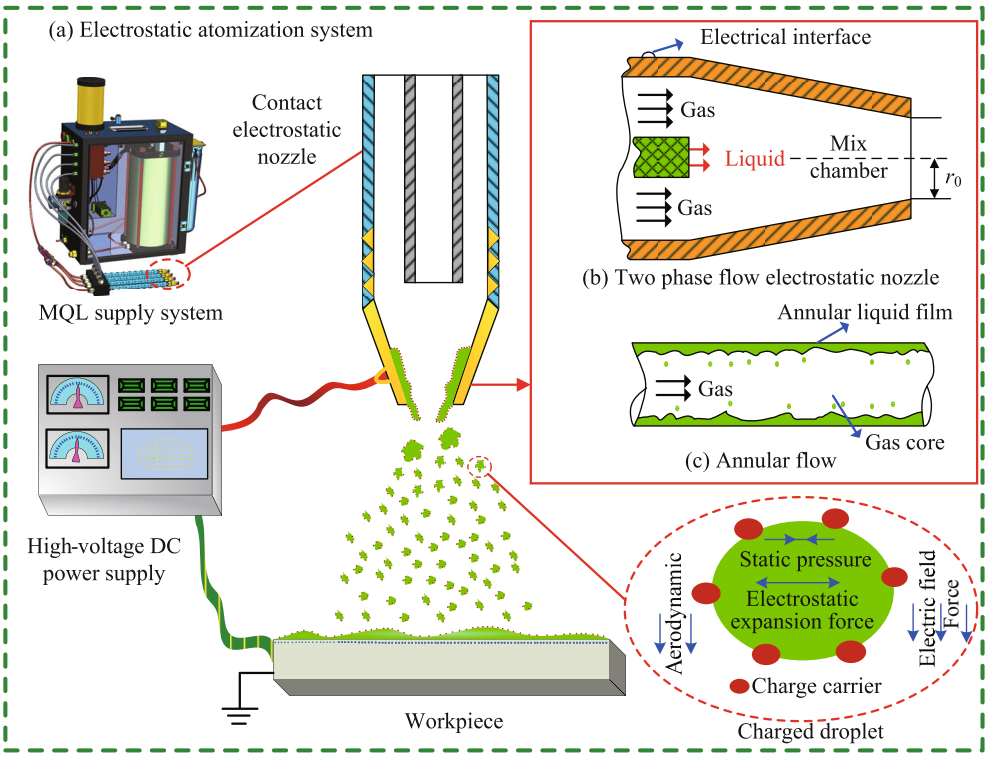

Fig. 1 Electrostatic atomization system and nozzle flow pattern. Note: r_0 is the radius of the nozzle outlet (m).

Fig. 1(b). Previously, Kim and Lee [47] conducted a visual experiment on the two-phase flow pattern in the pneumatic atomizer. The gas–liquid two-phase flow in the nozzle has an annular flow, i.e., the liquid flows along the nozzle wall, and the gas flows at a high speed in the center of the annular membrane to form a gas core, as shown in Fig. 1(c).

According to the surface instability theory, when liquid is ejected from the nozzle in continuous phase, a strong turbulence occurs between the liquid and the surrounding medium, thereafter producing unstable pressure fluctuations at the interface. With the continuous increase in external force, the fluctuation amplitude increases exponentially in time or space. When the amplitude is sufficiently large, the liquid breaks and forms an independent small liquid unit. Cherdantsev and Markovich [48] determined the gas core velocity in the annular liquid film to be large and the local sound velocity in the nozzle to be low. Thus, the gas core is in a state of pressure decrease and speed increase in the flow process. As the gas pressure at the outlet is higher than the external ambient pressure, the liquid will expand further, resulting in a further increase in velocity difference between gas and liquid. With the increase in velocity difference, the gas–liquid interface of the annular liquid membrane will produce a violent unstable fluctuation. Instability theory can help to derive the wave dispersion equations of the annular liquid film under various conditions. Furthermore, the correlation and proportion relationship between the average diameter of droplets and the longitudinal wavelength can be established based on the symmetrical or asymmetrical wave form of the liquid film [49, 50]. Wang et al. [51] and Zhang et al. [52], who studied longitudinal and transverse waves during liquid film rupture (Fig. 2), found lateral fluctuation as the main reason for the formation of a ligament structure at the nozzle outlet. The average diameter of droplets is also related to lateral wavelength size.

According to Daskiran et al. [53] and Vadivukkarasan and Panchagnula [54], shear force at the gas–liquid interface would lead to K–H instability, causing the liquid film to fluctuate longitudinally along the jet direction. The amplitude, growth rate, and wave number of longitudinal waves are mainly determined by the characteristics of liquid surface tension (σ) (N/m), gas phase, density, and velocity. Longitudinal

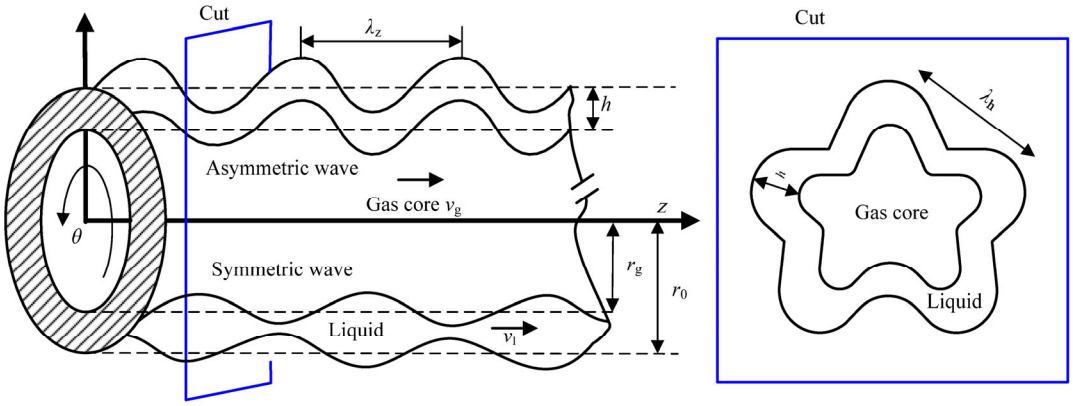

Fig. 2 Two-dimensional instability fluctuation of the annular liquid film. Note: v_g is the initial velocity of gas at the nozzle outlet (m/s), v_l is the liquid phase velocity (m/s), and r_g is the radius of the gas core (m).

waves can show the wave structure of the liquid film, and they mainly include symmetrical and asymmetrical waves. In general, the symmetrical fluctuation of the liquid film is more common in pneumatic atomizers. In addition, under the acceleration of external force, R–T instability occurs at the gas–liquid interface, resulting in the fluctuation of the liquid phase along the transverse direction of the nozzle. Transverse fluctuation is characterized by the formation of a wire drawing structure along the circumferential direction of the nozzle, also known as a braided structure. The amplitude, growth rate, and wave number of transverse waves are mainly determined by liquid density, acceleration, and surface tension (F_σ) (N). With the development and extension of the ligament in the jet direction, once the amplitude reaches a certain degree, the ligament breaks and forms multiple small liquid units. The small liquid unit eventually shrinks into spherical droplets under the action of surface tension or even further breaks under the action of external force. The smaller the liquid viscosity, the easier the annular liquid film is formed at the nozzle outlet, and the smaller the final droplet size [28].

Jin et al. [55] and Li et al. [56] conducted an in-depth research on the stability of coaxial electrofluid to explore the axisymmetric stability of the externally driven coaxial electrofluid in inviscid and viscous states. Grigo'ev and Shiryaeva [57] established a model of the pressure field and electric field under small disturbance and gave the dispersion equation of the small disturbance electrofluid in time mode. Bang et al. [58] deduced the dispersion equation of the charged cylindrical jet and studied the oscillation wavelength of the main unstable waves under different voltage conditions. Their results showed that the oscillation wavelength of the main unstable wave decreases with the increase in voltage. However, the stability analysis of the charged annular liquid film with high-speed gas core has not been reported.

3 Influence of jet parameters on charged annular liquid film

3.1 Particle image velocimetry (PIV) image data acquisition system

The atomization process of the internal mixing two-phase flow electrostatic atomizer is explored by collecting data about the formation and evolution process of the liquid's film instability structure near the nozzle outlet. Given the small-scale characteristics and short evolution period of the liquid film's interface disturbance structure, using ordinary equipment cannot sufficiently collect the transient structure information of the liquid film. Thus, in this study, high-speed micrography (i.e., PIV) technology is used to collect the information on transverse and longitudinal instability fluctuations, instability structure, and breaking shape of the annular liquid film near the nozzle outlet under different working conditions. The specific observation system is shown in Fig. 3. The acquisition system is mainly composed of the MQL system (FK TYPE MQL, Bluebe), high-voltage

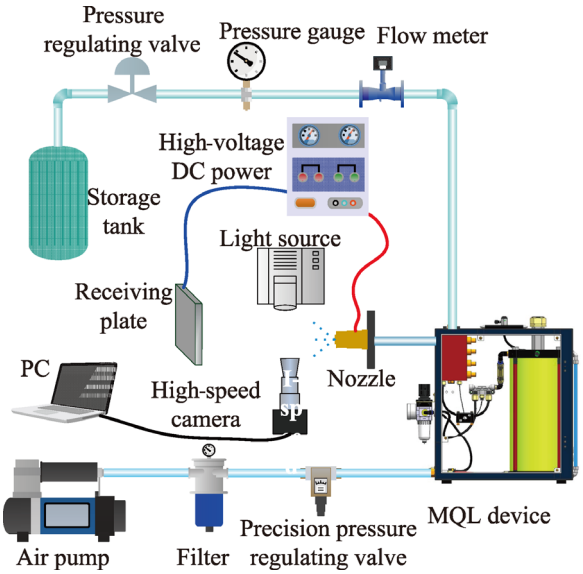

Fig. 3 PIV high-speed camera image acquisition system.

DC power supply (HDA-80T, Hongda), a gas supply system, a liquid supply system, a high-speed camera, a high-brightness light source, and a portable computer (PC) terminal. The model of high-speed camera is i-SPEED 221 (IX Camreas), and the light source is a light emitting diode (LED) high-intensity light source with continuously adjustable light intensity. The other parameters are also continuously adjustable: air supply pressure, between 0 and 0.8 MPa; liquid flow rate, between 0 and 200 mL/h; and voltage, between 20 and 60 kV. The electrostatic atomization process usually entails a large voltage; by contrast, the current between the two poles used in this study is at the micro-amp level, which is far lower than the safe current of 10 mA [59]. The radius of the nozzle outlet (r_0) is 1×10^{-3} m, the atomized liquid is soybean oil, and the average flow rate is adjusted to 60 mL/h. The distance between the receiving plate and nozzle is 0.05 m.

3.2 Effect of air pressure on liquid film instability

The effect of air pressure on the instability of the annular liquid film during the atomization of the internal mixing two-phase flow nozzle is analyzed by collecting images of the annular liquid film at the nozzle outlet under different air pressure conditions (0.1, 0.2, 0.3, and 0.4 MPa) at 0 kV (pure pneumatic atomization). The annular liquid film before the formation of the ligament at the nozzle outlet is shown in Fig. 4. In pure pneumatic atomization mode, the liquid film at the nozzle outlet is transversely unstable under the action of air flow, which is manifested as a circumferential wave along the nozzle. When the air pressure is 0.1 MPa, the nozzle outlet appears with two peaks. With the increase in gas pressure, the transverse fluctuation of the liquid film tends to further intensify. Moreover, the wave number increases, the λ_h decreases, and the distribution between peaks tends to be more uniform. As the nozzle is placed horizontally, the liquid under the nozzle is significantly more than the liquid above the nozzle under the action of gravity. The smaller the gas pressure, the more obvious this phenomenon.

Figure 5 shows the shapes and distributions of the ligament at the nozzle outlet. Under the action of gas drag, the liquid film pulls out multiple ligaments at the transverse wave crest and develops along the jet direction. Under the action of gas shear force, the ligament fluctuates longitudinally and propagates downstream. When the gas pressure is small, the

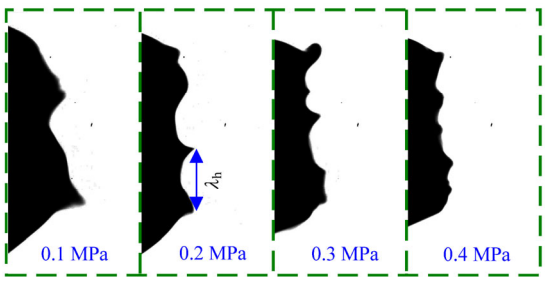

Fig. 4 Transverse fluctuations of the liquid film at the nozzle outlet under different pressure conditions.

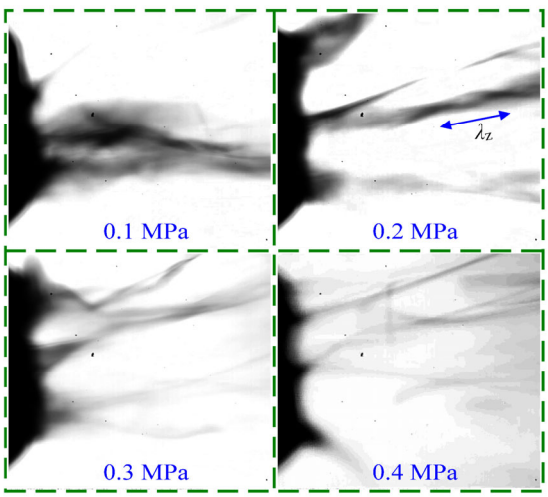

Fig. 5 Ligament distributions and morphologies at the nozzle outlet under different pressure conditions.

number of formed transverse wave peaks is small, the number of ligaments at the outlet is small, and the diameter of the ligament is large. With the increase in gas pressure, the number of ligaments increases, while its diameter decreases continuously, and the distribution of ligaments tends to be uniform. Longitudinal fluctuations occur on the ligament surface. However, the λ_z is difficult to quantitatively characterize because of the turbulence between gas and liquid.

The analysis shows an extremely complex wave even on the same ligament due to the superposition of waves. Although many scholars have studied the longitudinal wavelength of jets, the longitudinal wavelength of the liquid film under the height of the gas–liquid two-phase flow cannot be determined accurately. Increasing the gas pressure will aggravate the disturbance of the gas–liquid interface, reduce the longitudinal wavelength, and increase the propagation speed and growth rate of the wave. Furthermore, the fracture length of the ligament is proportional to the longitudinal wavelength. In the case of symmetric waves, two waves meet at the wave trough, and the ligament breaks into two equal parts with the same wavelength; therefore, the half-wavelength is often used to calculate droplet size. Figure 5 shows a high frequency of symmetrical fluctuations, excluding the complex ones. With the increase in air pressure, the breaking length of the ligament decreases continuously. This phenomenon can be explained by the increase in gas velocity, which increases the amplitude of the wave and accelerates the propagation speed.

3.3 Effect of voltage on liquid film instability

When the air pressure is 0 MPa, and the voltage is 40 kV, the shape of the liquid film is arranged vertically at the nozzle outlet (Fig. 6). Under the action of electrostatic force, the liquid film at the nozzle outlet has a unique Taylor cone structure for the electric jet. Under the traction of the electric field, ligaments and monodisperse droplets appear at the tip of the Taylor cone. In electrostatic three-dimensional printing, the capillary tube is used as a nozzle, and liquid atomization is realized using an electric field. When the diameter of the EMQL nozzle is much larger than that of the capillary tube, simply using electrostatic fluid cannot achieve the processing requirements of high atomization. Therefore, gas is needed for auxiliary atomization.

The influence of the coupling effect of air flow field and electrostatic field on the instability of the annular liquid film is studied via an experiment that requires a collection of image information of the annular liquid film at the nozzle outlet under different conditions of air pressure (0.1, 0.2, 0.3, and 0.4 MPa) and voltage (0, 20, 25, 30, 35, and 40 kV). The shapes of the liquid film under different voltage conditions with an air pressure of 0.2 MPa are shown in Fig. 7. With the increase in voltage, the transverse fluctuation of the liquid film tends to further intensify, the wave number increases, the transverse wavelength decreases, and the distribution between wave peaks is more

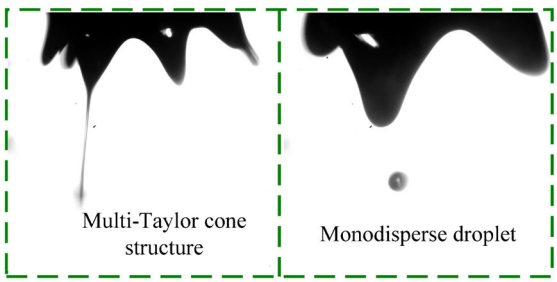

Fig. 6 Morphologies of the liquid film at the nozzle outlet under the 0 MPa/40 kV condition.

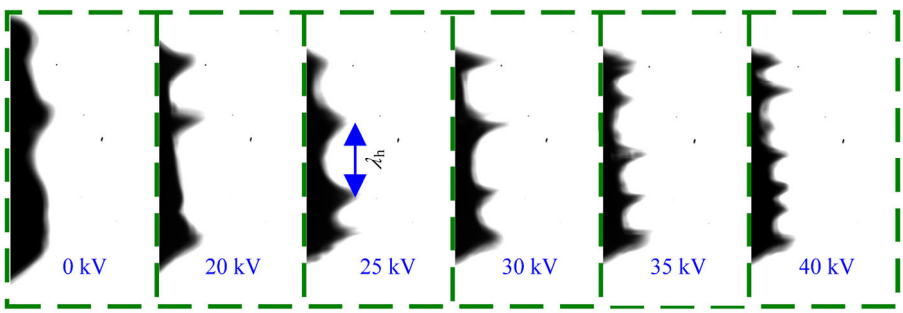

Fig. 7 Transverse fluctuations of the liquid film at the nozzle outlet under different voltage conditions.

uniform. This trend can be attributed to the liquid surface having the same charge, causing the surface layer to have a significant directional arrangement, thereafter reducing the σ and liquid deformation resistance. Furthermore, after the liquid is charged, additional electrical disturbance occurs at the gas–liquid interface. In particular, after the nozzle is energized, a Taylor cone structure appears at the front end of the liquid film, which is a unique structural feature of the electric jet. This phenomenon proves the obvious effect of the electric field on the transverse fluctuation of the liquid film. The electric traction at the wave crest is greater under the action of electric field force because of the denser charge distribution at the wave crest on the liquid film surface. Under the action of electroviscous effect, the charge moves the nearby liquid microclusters, subsequently forming a Taylor cone structure. In addition, after the nozzle is charged, the liquid deposition at the bottom of the nozzle under the influence of gravity is significantly improved. This phenomenon can be explained by the liquid spreading more evenly along the inner wall of the nozzle under the action of Coulomb repulsion after charging.

Figure 8 shows the shapes and distributions of the liquid line at the nozzle outlet under different voltage conditions with an air pressure of 0.2 MPa. Under the synergistic action of gas drag and electrostatic force, the liquid film is pulled out from the tip of the Taylor cone to form ligaments. The diameter of the ligament at the nozzle outlet is smaller than that under the pure pneumatic atomization condition despite the same pressure value. As the voltage rises, the number of ligaments increases, the diameter of the ligament decreases, and the distribution of ligaments tends to be more uniform. Under the traction of electric field force, the longitudinal movement speed of ligaments increases, and the liquid breaking speed increases. Therefore, the breaking length of ligaments decreases with the increase in voltage. When the voltage is 35 kV, some ligaments break near the outlet. When the voltage reaches 40 kV, all ligaments near the outlet rupture. If the ligament velocity is fast, and the diameter is small, then the fluctuation of the ligament surface is difficult to directly observe. Thus, the single coarse ligament image formed at the nozzle outlet is collected in the experiment. The surface fluctuation of the ligament is symmetrical.

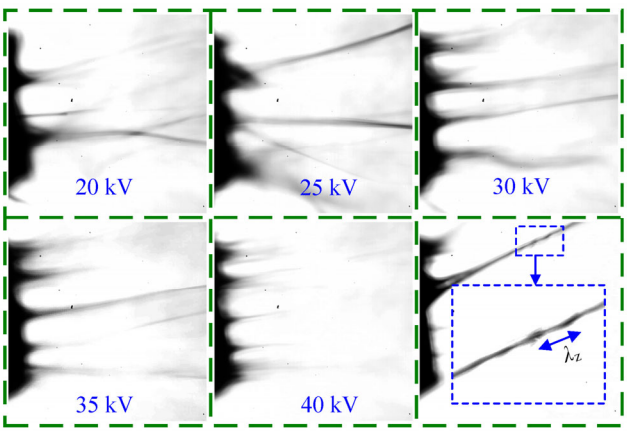

Fig. 8 Ligament distributions and morphologies at the nozzle outlet under different voltage conditions

4 Mathematical model of volume average particle size of charged droplets

The existing mathematical model of droplet size only considers one-dimensional longitudinal fluctuation. However, a large error exists between the theoretical predicted particle size and the real particle size. In PIV observation experiments, the fluctuation of the gas–liquid interface is a highly complex phenomenon, and the breaking process of the liquid film is a three-dimensional problem. The longitudinal wavelength, transverse wavelength, and thickness of the liquid film all have effects on the average diameter of droplets [60]. Figure 9 depicts a case of a local nozzle outlet expanded into a plane and the related liquid film distribution and its breaking process. The liquid

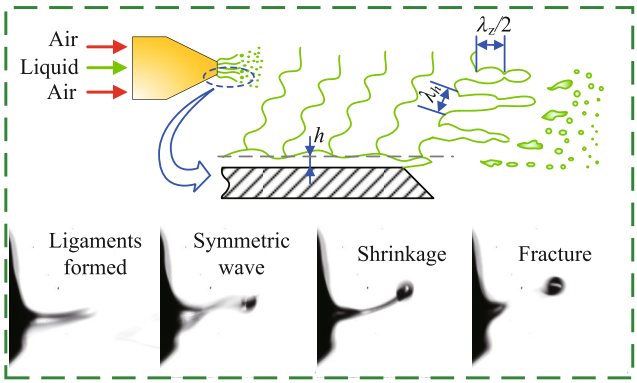

Fig. 9 Three-dimensional breaking mechanism of the annular liquid film.

film pulls out a ligament at each transverse wave peak, and the longitudinal wave at the ligament interface is symmetrical. The ligament shrinks at the longitudinal half-wavelength to form a small liquid unit, further breaking and shrinking into spherical droplets under the action of surface tension.

In summary, the average droplet volume diameter at the nozzle outlet is directly proportional to the longitudinal half-wavelength, transverse wavelength, and thickness of the liquid film. A three-dimensional equal-volume mathematical model of annular membrane crushing atomization can be constructed according to the principle of constant volume in the liquid crushing process. The VAD is given by Eq. (1):

$$\mathrm{VAD} = \sqrt[3]{\frac{3h\lambda_z\lambda_h}{\pi}} \tag{1}$$

4.1 Liquid film thickness

The existing liquid film thickness model is mainly based on Bernoulli's law of horizontal tube. This kind of model uses the change in gas pressure inside and outside the nozzle to calculate the liquid phase velocity (v_l) (m/s), and it ignores the pressure drop caused by friction and gravity on the inner wall of the nozzle. The model cannot reflect the effect of electric field intensity on liquid phase velocity. Furthermore, as the nozzle structure is much more complex than the horizontal tube, a large deviation usually occurs for the predicted value of the model.

This study defines the void fraction (α) of the annular liquid film at the outlet of two-phase flow nozzle as the ratio of the cross-sectional area of the gas core to the cross-sectional area of the nozzle outlet. It is given by Eq. (2):

$$\alpha = \frac{r_g^2}{r_0^2} \tag{2}$$

where r_g is the radius of the gas core (m).

For the EMQL two-phase flow nozzle in pulse liquid supply mode, its duty cycle (ratio of oil delivery time to non-oil delivery time) is 1:5. The instantaneous mass flow (m_l') (kg/s) is obtained from the average mass flow of the microlubricant. If the liquid velocity and liquid density at the nozzle outlet are known, then the void fraction can be derived as

$$m_l' = \rho_l v_l \pi r_0^2 (1-\alpha) \tag{3}$$

where ρ_l is the liquid phase density (kg/m^3). According to the above analysis, the nozzle outlet is an annular liquid film. The annular liquid film thickness is given by Eq. (4):

$$h = r_0\left(1-\sqrt{\alpha}\right) \tag{4}$$

The liquid phase velocity in the model needs to be obtained. Here, the continuous image information of the outlet liquid film is obtained using a high-speed camera system.

4.2 Longitudinal wavelength

The longitudinal wavelength of the liquid film under the condition of high-speed gas-assisted jet atomization is analyzed according to the theory of surface instability. Then, the effects of physical properties, such as gas and liquid velocity, density, gas compressibility, liquid viscosity, surface tension, and boundary conditions, on longitudinal wavelength are considered based on the principles of mass conservation and momentum conservation in gas phase and liquid phase. By introducing a stream function and a velocity potential function in the cylindrical coordinate system, the interface longitudinal wave dispersion equation can be constructed to reveal the implicit relation between the surface wave growth rate (ω) and surface wave number (k) or wavelength (λ) (m). When the gas–liquid interface is a velocity discontinuous interface, the vortex thickness tends to be zero. Here, the liquid phase density is considered to be much higher than the gas phase density ($\rho_l \gg \rho_g$). According to the K–H wave instability theory [48], the dispersion equation of the interface disturbed by gas and liquid is

$$\omega = k\frac{\rho_l v_l + \rho_g v_g}{\rho_l + \rho_g} \pm i\frac{k}{\rho_l + \rho_g}\sqrt{\rho_l\rho_g(v_g - v_l)^2 - (\rho_l + \rho_g)\sigma k} \tag{5}$$

where i is the imaginary part. The maximum growth rate (ω_{max}) is calculated as

$$\omega_{max} = \frac{2}{3\sqrt{3}}\left(\frac{\rho_g}{\rho_l}\right)^{\frac{1}{2}}\frac{\rho_g v_g^3}{\sigma} \tag{6}$$

In Eqs. (5) and (6), the surface wave number corresponding to the maximum growth rate is given by

$$k = \frac{2\rho_g v_g^2}{3\sigma} \tag{7}$$

where v_g is the initial velocity of gas at the nozzle outlet (m/s). Then, by considering the relationship between wavelength and wave number, the main unstable wavelength (λ_{KH}) (m) of the surface wave can be obtained as

$$\lambda_{KH} = \frac{2\pi}{k} = \frac{3\pi\sigma}{\rho_g v_g^2} \tag{8}$$

Without considering the influence of gravity, droplets tend to shrink into ideal spheres with radii (R) (m) under the action of surface tension. The static pressure (P_s) (N) is generated inside and outside the droplet, as shown in Fig. 10(a). When the droplet is charged, the charge is distributed on the droplet surface because of the skin effect, a phenomenon that can be simplified as a surface charge model. Under the action of the same charge repulsion on the surface, the electrostatic expansion force (P_e) (N) opposite to the static pressure is generated inside the droplet, as shown in Fig. 10(b).

Assuming that the charged droplet is an ideal sphere, and the surface is non-fluctuating, the total electricity (Q_d) (C) carried by the droplet is evenly distributed on this droplet's outer surface. According to the principle of electrostatic field superposition, the electric field intensity of r_s point (E_s) (V/m) at any distance outside the droplet can be calculated as

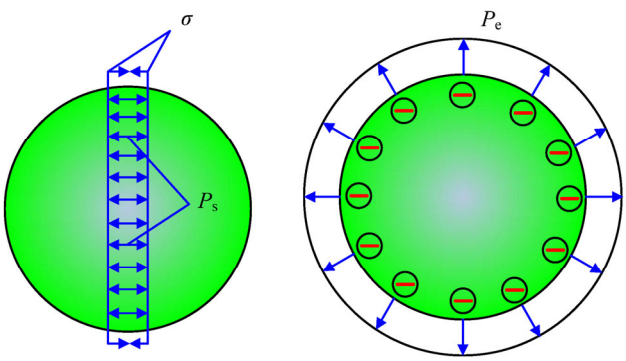

(a) Hydrostatic pressure (b) Electrostatic expansion pressure

Fig. 10 Force analysis of the charged droplet.

$$E_s = \frac{Q_d}{4\pi\varepsilon_r\varepsilon_0 r_s^2} \tag{9}$$

where r_s is the distance from the calculation point to the center of the sphere (m). The surface potential of the spherical droplets and the electrostatic energy stored by these droplets can be expressed as

$$U_d = -\int_{\infty}^{R} E_s \mathrm{d}r_s = \frac{Q_d}{4\pi\varepsilon_r\varepsilon_0 R} \tag{10}$$

$$W_e = \int_0^{Q_d} U_d \mathrm{d}Q_d = \frac{Q_d^2}{8\pi\varepsilon_r\varepsilon_0 R} \tag{11}$$

where U_d is the droplet surface potential (V), and W_e is the electrostatic energy stored by the droplet (J). Assuming that the reduction of surface tension caused by droplet charging is the surface tension reduction ($\Delta\sigma$) (N/m), the corresponding surface energy variation of droplets is

$$\Delta W_s = 4\pi\Delta\sigma R^2 \tag{12}$$

where ΔW_s is the surface energy variation of the droplet (J). At this time, the total energy of the droplet is $W = W_e + \Delta W_s$. The following relationship can be derived from the principle of virtual work.

$$\frac{\mathrm{d}W}{\mathrm{d}R} = -\frac{Q_d^2}{8\pi\varepsilon_r\varepsilon_0 R^2} + 8\pi\Delta\sigma R = 0 \tag{13}$$

where

$$\Delta\sigma = \frac{Q_d^2}{64\pi^2\varepsilon_r\varepsilon_0 R^3} \tag{14}$$

If $\sigma = \Delta\sigma$, then the static pressure generated by surface tension is completely offset by the electrostatic expansion force. At this time, the droplets would be deformed and broken. By considering the critical conditions and Eq. (14), σ can be further expressed as

$$\sigma = \frac{Q_{Cr}^2}{64\pi^2\varepsilon_r\varepsilon_0 R^3} \tag{15}$$

where Q_{Cr} is the limit charge of droplets (C). Q_{Cr} in Eq. (15) is substituted as

$$Q_{Cr} = 8\pi\sqrt{\sigma\varepsilon_r\varepsilon_0 R^3} \tag{16}$$

The limit charge of the droplet is considered in this study. The limit charge mass ratio (C_{Cr}) (C/kg) is expressed as

$$C_{Cr} = 6\sqrt{\frac{\sigma\varepsilon_r\varepsilon_0}{R^3\rho_l^2}} \tag{17}$$

When the true charge of the droplet is less than the limit charge, the droplet is in a stable state. The effective surface tension of charged liquid (σ^*) (N/m) is given by Eq. (18):

$$\sigma^* = \sigma - \frac{Q_d^2}{64\pi^2\varepsilon_r\varepsilon_0 R^3} \tag{18}$$

The formulation of the relationship between the effective surface tension of charged liquid and the true charge mass ratio is

$$\sigma^* = \sigma - \frac{C_z^2 R^3 \rho_l^2}{36\varepsilon_r\varepsilon_0} \tag{19}$$

The outlet of the internal mixing two-phase flow electrostatic nozzle is an annular liquid film, and it needs to be transformed into an equal-volume sphere. The volume of the annular liquid film (V_l) (m^3) can be expressed as

$$V_l = \pi\left(r_0^2 - r_g^2\right)L \tag{20}$$

where L is the length of the annular liquid film (m). The edge of the annular liquid film is irregular due to the existence of transverse fluctuation on the liquid film surface. As the length of the liquid film cannot be measured directly, fitting calculations are required. After removing the lens stain on the image, it is transformed into a binary image. The first black pixel is approached from the top, bottom, and right directions, and the liquid film calculation area at the nozzle outlet is automatically intercepted, as shown in Fig. 11. The proportion of black pixels is calculated based on the total number of pixels and black pixels in the rectangular area. Then, from the ratio of pixel value to actual size, the equivalent length of the annular liquid film (L') (m) is calculated.

Different air pressure and voltage conditions are considered in this study. Twenty images for each working condition are utilized in the analysis, and the average value is calculated. The equivalent length of the liquid film under all working conditions is between 0.264 and 0.291 mm. The equivalent length variation is negligible under different working conditions. Subsequently, 0.276 mm is selected as the equivalent length of the liquid film for all working conditions. The equal-volume spherical diameter of annular liquid film (R') (m) is expressed as

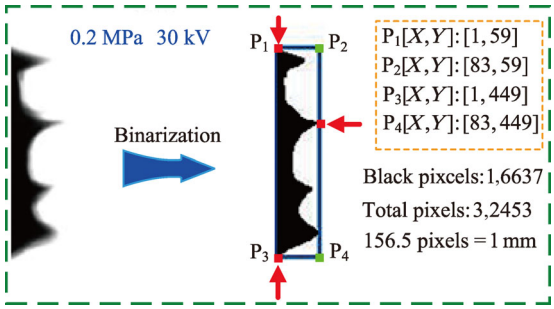

Fig. 11 Calculation scheme for deriving the equivalent length of the liquid film.

$$R' = \sqrt[3]{0.75\pi\left(r_0^2 - r_g^2\right)L'} \tag{21}$$

Equations (19)–(21) are substituted to express the effective surface tension of charged liquid.

$$\sigma^* = \sigma - \frac{C_z^2\left(r_0^2 - r_g^2\right)L'\rho_l^2}{48\varepsilon_r\varepsilon_0} \tag{22}$$

According to Eq. (8), the longitudinal wavelength of the annular liquid film after surface tension can be reduced as

$$\lambda_z = \frac{3\pi\sigma^*}{\rho_g v_g^2} \tag{23}$$

4.3 Transverse wavelength

When the density of the liquid phase is much higher than that of the gas phase, the interface disturbance caused by various types of acceleration can be represented as an R–T unstable wave. The most unstable wavelength of the R–T wave (λ_{RT}) (m) can be calculated as [48]:

$$\lambda_{RT} = 2\pi\left(3\sigma / \rho_l a\right)^{1/2} \tag{24}$$

where a is the acceleration of the liquid at the nozzle outlet (m/s^2).

In the process of electrostatic atomization, the annular liquid film at the nozzle outlet is mainly affected by gas drag, electrostatic field force (F_e) (N), and surface tension. The gas drag force (F_g) (N) and electrostatic field force accelerate the movement of the liquid film downstream of the nozzle, but surface tension hinders the liquid film's downstream movement. According to the stress analysis of the annular membrane

$$m_l a = F_g + F_e - F_\sigma \tag{25}$$

where m_l is the mass of the liquid film at the nozzle outlet (kg). The mass of the liquid film is calculated as

$$m_l = \pi\left(r_0^2 - r_g^2\right)L'\rho_l \tag{26}$$

According to the theory of fluid mechanics, the gas drag can be expressed as

$$F_g = \frac{1}{2}C_D\rho_g v_r^2 S_l \tag{27}$$

where C_D is the drag coefficient, v_r is the relative velocity of gas and liquid in the nozzle (m/s), and S_l is the windward area of the annular liquid film (m^2).

The nozzle and receiving surface are two conductive electrodes filled with dielectric material (air) and can jointly act as a capacitor [61]. The charged amount of the nozzle liquid film is given by Eq. (28):

$$Q_z = \frac{\varepsilon_r\varepsilon_0 S_n}{d}U = \frac{\varepsilon_r\varepsilon_0\pi\left(r_p^2 - r_0^2\right)}{d}U \tag{28}$$

where Q_z is the charge of the liquid film (C), ε_r is the relative permittivity of air (i.e., 1.00053), ε_0 is the dielectric constant of vacuum (i.e., 8.85×10^{-12} C/V·m), S_n is the area directly opposite the two poles (m^2), U is the nozzle voltage (V), and d is the relative distance between electrodes (m). According to Eq. (28), the electrostatic force on the liquid film can be expressed as

$$F_e = E_d Q_z = \frac{\varepsilon_r\varepsilon_0 S_n}{d^2}U^2 \tag{29}$$

where E_d is the electric field intensity between electrodes (V/m). The resultant force of surface tension on the liquid film is

$$F_\sigma = 2\pi\left(r_0 + r_g\right)\sigma^* \tag{30}$$

According to Eqs. (24)–(30), the λ_h can be expressed as

$$\lambda_h = 2\pi\sqrt{\frac{3m_l\sigma^*}{\rho_l\left(F_g + F_e - F_\sigma\right)}} \tag{31}$$

In conclusion, by considering the liquid film thickness (Eq. (4)), transverse wavelength (Eq. (31)), and longitudinal wavelength (Eq. (23)), the VADs of the droplets can be calculated as

$$D = \sqrt[3]{6r_0\left(1-\sqrt{\alpha}\right)\left(\frac{3\pi\sigma^*}{\rho_g v_g^2}\right)\sqrt{\frac{3m_l\sigma^*}{\rho_l\left[\frac{1}{2}C_D\rho_g v_r^2 S_l + 2\pi\left(r_0+r_g\right)\sigma^* - 2\pi\left(r_0+r_g\right)\sigma^*\right]}}} \tag{32}$$

5 Mathematical model calculation and error analysis

5.1 Determination of the input parameters of the mathematical model

The liquid phase velocity, gas core velocity, and droplet charge mass ratio under different air pressure and voltage conditions must be provided to be able to compute the final VAD of the mathematical model. The liquid phase velocity can be obtained by analyzing the nozzle liquid film image collected in the PIV experiment. The steps are briefly given as follows: The continuous liquid film image is selected, and a binary image is turned. The first black pixel from the right side of the image is approached, and the coordinate value is obtained. Similarly, the X-coordinate values of the rightmost black pixel in the continuous images are selected, as shown in Fig. 12. The X-coordinate value difference of the rightmost black pixel of two consecutive images as the moving distance of the liquid film is taken. Here, the time interval between consecutive images is 0.002 s. Finally, the liquid phase velocity at the nozzle outlet based on the ratio of pixel value to actual size is obtained.

Twenty continuous images are selected for analysis, and the average value under different compressed air

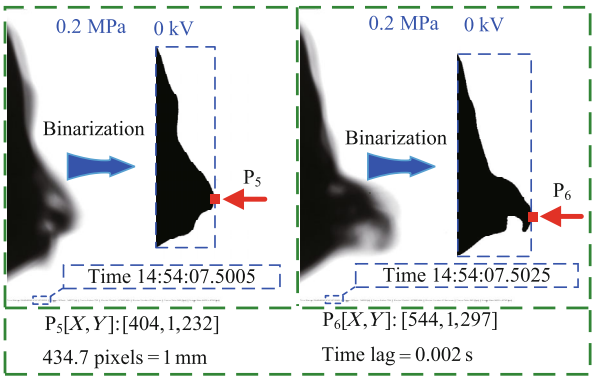

Fig. 12 Calculation scheme of liquid film velocity at the nozzle outlet.

pressure (P) (MPa) and U (kV) conditions is calculated. On this basis, the liquid phase velocity at the nozzle outlet can be obtained, as shown in Table 1. The liquid phase velocity increases with the rise in air pressure and voltage, which can be attributed to the effect of gas drag and electric field traction.

The total charge of droplets per unit time is measured using the charge meter (EST111, Beijing Jingbeinuo Technology Co., Ltd.) and Faraday cylinder. The average charge mass ratio is obtained by measuring the total mass of droplets per unit time. The surface tension of soybean oil is measured using the surface tension meter (BZY - 201, Shanghai Fangrui Instrument Co., Ltd.). Here, the voltage is assumed to have no effect on the gas core velocity. The gas volume at the nozzle outlet is measured using a vortex flowmeter, and the initial gas velocity under various working conditions is calculated according to the measured pipeline diameter.

5.2 Calculation results of the mathematical model

The surface tension of soybean oil at room temperature is 32.17 mN/m. The values of initial gas velocity (v_g) are 38.25, 56.38, 69.40, and 79.92 m/s under different conditions between 0.1 and 0.4 MPa. The corresponding measurements of real charge mass ratio (C_z) and $\Delta\sigma$ are shown in Figs. 13 and 14, respectively. Given the same air pressure condition, C_z and $\Delta\sigma$ increase with the rise in voltage. The amplitudes of the two changes decrease with the increase in voltage. The trends indicate that increasing the voltage tends to saturate the liquid charge, hindering the liquid to charge further. Furthermore, given the same voltage condition, C_z and $\Delta\sigma$ decrease with the increase in air pressure. This phenomenon can be explained by the liquid phase velocity rising with the increase in air pressure, thereafter decreasing the contact charging time between the liquid phase and nozzle. When the air pressure is 0.1 MPa, and the voltage is 40 kV, the maximum C_z and $\Delta\sigma$ are 0.3078 mC/kg and 8.3301 mN/m, respectively. At 0.4 MPa and 20 kV, the minimum C_z and $\Delta\sigma$ are 0.1556 mC/kg and 1.6986 mN/m, respectively.

Table 1 Liquid velocity at the nozzle outlet (m/s) under different voltage and pressure conditions.

P (MPa) \ U (kV)	0	20	25	30	35	40
0.1	0.1357	0.1772	0.1855	0.1918	0.1954	0.1978
0.2	0.1692	0.1984	0.2063	0.2120	0.2151	0.2179
0.3	0.2084	0.2341	0.2412	0.2464	0.2490	0.2511
0.4	0.2256	0.2479	0.2547	0.2595	0.2619	0.2637

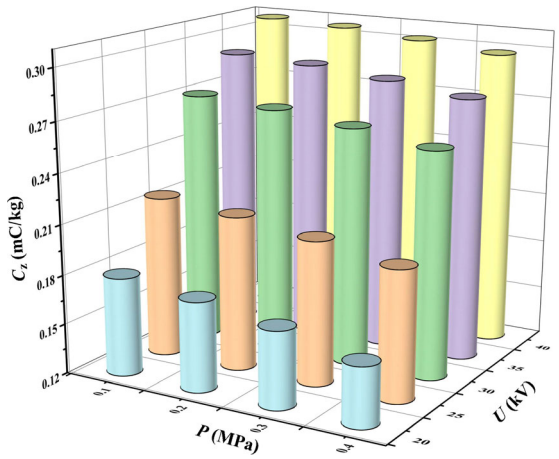

Fig. 13 Charge mass ratios under different conditions.

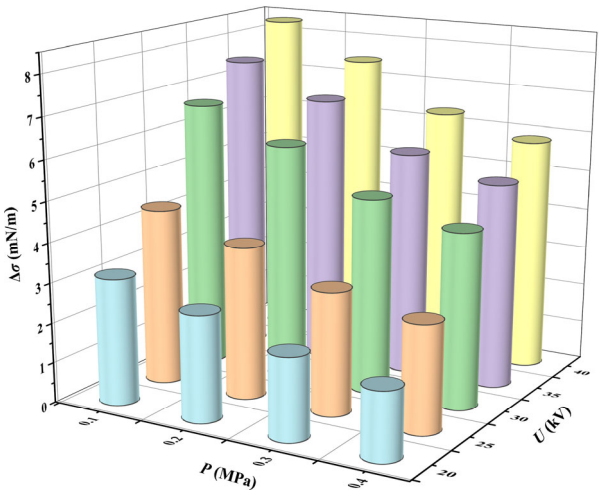

Fig. 14 Variations of surface tension under different conditions.

The h (62.3–125.2 μm), λ_z (32.4–172.7 μm), λ_h (457.4–1,700 μm), and theoretical VADs (95.9–327.4 μm) under different working conditions are determined by substituting the abovementioned input parameters into the mathematical model. The specific results are shown in Figs. 15(a) and 15(b). The variations of transverse wavelength, longitudinal wavelength, and thickness of the liquid film and the VADs of the droplets with respect to air pressure and voltage are all consistent. Thus, the gas drag force and electric field drag force of the liquid film increase continuously as the air pressure and voltage increase. This situation further leads to the increase in liquid phase velocity at the nozzle outlet and the decrease in liquid film thickness. The influence of gas traction on the liquid phase velocity is more obvious compared with the influence of electric field traction. The longitudinal wavelength of the annular liquid membrane decreases with the increase in air pressure and voltage. The effect of voltage on longitudinal wavelength is depicted by the decrease in surface tension of the liquid after it is charged, causing the deformation resistance of the liquid to be decreased. Meanwhile, the increase of gas velocity will cause the increase of external force of liquid deformation. Notably, increasing the gas phase velocity reduces the contact time between the liquid phase and nozzle, and it has a negative impact on the charge of the liquid. Furthermore, the transverse wavelength of the annular liquid film decreases with the increase in air pressure and voltage. The influence of voltage on transverse wavelength is reflected in two aspects. On the one hand, the increase in voltage reduces the surface tension of the liquid, eventually reducing its deformation resistance. On the other hand, the increase in voltage increases the traction force of the electric field, thereafter accelerating the liquid phase acceleration. Both of these phenomena reduce the transverse wavelength. Similarly, the increase in air pressure further accelerates the liquid phase, which is manifested by the decrease in transverse wavelength. Here, the maximum values of the transverse wavelength, longitudinal wavelength, and thickness of the liquid film are obtained at 0.1 MPa/0 kV, whereas the corresponding minimum values are obtained at 0.4 MPa/40 kV. The VADs of the droplets are affected by the thickness and transverse and longitudinal wavelengths of the liquid film. Consequently, the VADs of the droplets decrease with the increase in air pressure and voltage. The values of transverse wavelength are significantly larger than those of liquid film thickness and longitudinal wavelength, further suggesting that transverse wavelength may have a greater impact on particle size. In other words, the number and distribution of ligaments have the most obvious effect on the VADs of the droplets.

5.3 Model verification and error analysis

Regarding the error of the mathematical model, the experimental values of the VADs of the droplets under different working conditions need to be measured for comparison and verification. The laser particle sizer (Winner319, Jinan Micro-nano Particle Instrument Co., Ltd.) is used to collect and measure the VADs of the droplets and their diameter distribution characteristics. Its working principle is shown in Fig. 16. The transmitter

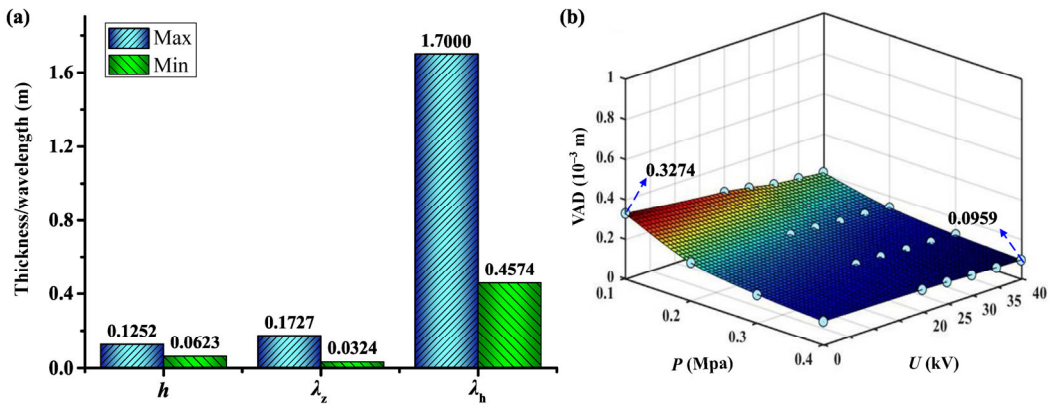

Fig. 15 Different air pressure and voltage conditions: (a) thickness, longitudinal wavelength, and transverse wavelength of the liquid film; (b) VADs of droplets.

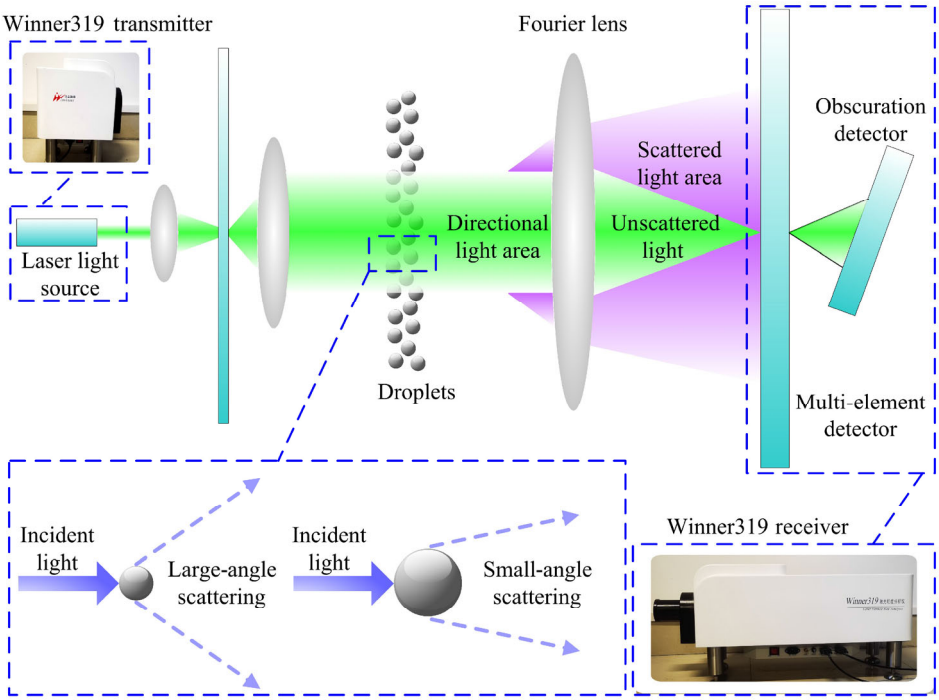

Fig. 16 Working principle of the laser particle size analyzer.

sends a monochromatic parallel laser, and the beam vertically enters the droplet test area after passing through the lens. Droplets with different particle sizes cause the parallel beam to manifest a polydispersive Fraunhofer diffraction behavior. The diffraction angle produced by large diameter droplets is small, whereas the diffraction angle produced by small diameter droplets is large. Once the diffracted beam reaches the detector at the receiving end, the particle size distribution and the VADs of the droplets can be finally obtained using an energy spectral analysis apparatus. The laser particle sizer is used to obtain the R.S value of the particle sizes' distribution span and the percentage concentrations of PM10 and PM2.5. In consideration of the influence of the nozzle on the detection beam, the position 10 mm away from the nozzle outlet is selected as the atomization measurement point.

The value of the droplet diameter variable in Eq. (32) is a discrete value. Here, the obtained discrete values are processed by polynomial fitting. The fitted adjusted *R*-square value is between 0.977 and 0.989; the fitting accuracy is regarded as sufficient in this study. Figure 17 shows a comparison between the calculated VADs of the droplets and the experimental values. The variation trend of the VADs of the droplets with respect to voltage and air pressure is consistent with that of the theoretical calculation. When the air pressure is 0.1–0.3 MPa, the errors of pure pneumatic atomization are greater than those of electrostatic atomization (i.e., 8.76%, 1.91%, and 8.78%). At 0.1 MPa and 20–40 kV, the error is between 3.38% and 4.79%. At 0.2 MPa and 20–40 kV, the error is between 0.01% and 1.05%. At 0.2 MPa under the charged condition, the calculated value is the closest to the experimental

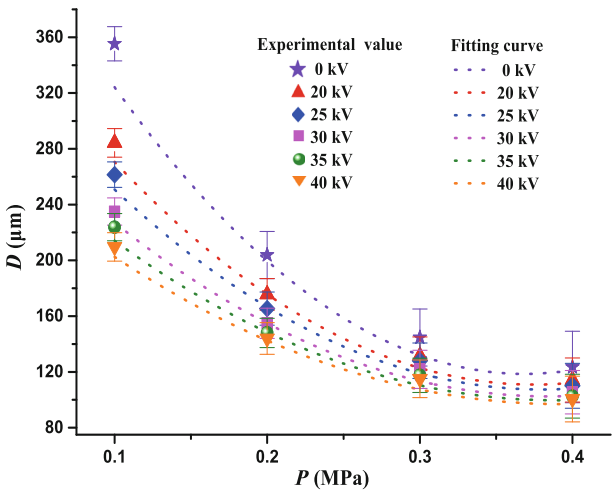

Fig. 17 Comparison between the calculated and measured values of the average droplet diameter.

value. At 0.3 MPa and 20–40 kV, the error is between 6.10% and 7.04%. When the air pressure is 0.4 MPa, the error value of pure pneumatic atomization is 1.72%. At 0.4 MPa and 20–40 kV, the error value is between 1.70% and 3.55%. Figure 17 shows the standard deviations of the derived values. The increase is significant in terms of the randomness of liquid atomization with respect to the increase in air pressure. The randomness of liquid atomization decreases, while the controllability increases with the increase in voltage.

6 Atomization characteristics

6.1 Droplet diameter distribution span R.S

The research on the atomization quality of nozzles not only pays attention to the average diameter of droplet groups but also their respective particle size distributions. The more concentrated the droplet distribution, the closer the particle size between droplets, and the higher the controllability of atomization parameters. The effects of the aerodynamic and electrical parameters on the diameter distribution and concentration of fine droplets in the atomization process are studied by collecting data on the span value R.S and PM10/PM2.5 percentage concentrations under different working conditions. The droplet diameter distribution is characterized by the span value R.S. The R.S value is calculated according to $(x_{90} - x_{10})/x_{50}$, where x_{90}, x_{10}, and x_{50} mean the diameters of 90%, 10%, and 50% of the measured cumulative distribution of droplets (i.e., the volume contents of droplets smaller than this diameter account for 90%, 10%, and 50% of all droplets), respectively. The larger the R.S value, the wider the droplet diameter distribution range, and the higher the degree of non-uniformity of droplets. Figure 18 shows the measured cumulative distribution curves of the droplets at 0.3 MPa.

When the air pressure is 0.3 MPa, and the voltage is 0 kV, the droplet diameter size distribution is extremely wide, and the R.S value reaches 2.982. After the nozzle is energized, the droplet diameter distribution narrows with the increase in voltage. When the voltage is 40 kV, the minimum R.S value of 1.697 is obtained, which is a reduction by 43.09% compared with that under the pure pneumatic atomization condition at 0.3 MPa.

Figure 19 shows the scatter distributions of the R.S values measured experimentally under different working conditions. Under the pure pneumatic atomization condition, R.S has an obvious upward trend with the increase in air pressure. When the air pressure is 0.4 MPa, R.S is 3.363. When the air pressure is 0.2 and 0.4 MPa, the change trend of R.S is consistent with that at 0.3 MPa. The R.S at 0.2 MPa/40 kV is 19.7% lower than that at 0.2 MPa/0 kV. Furthermore, the R.S at 0.4 MPa/40 kV is 45.38% lower than that at 0.4 MPa/0 kV. The analysis indicates that with the increase in voltage, the liquid film spreads more evenly at the nozzle outlet, the transverse fluctuation tends to further intensify, and the transverse wave crest is denser. Therefore, the droplet diameter distribution is more concentrated, and the probability of generating droplets with large and small diameters is reduced. This finding further suggests that the uniformity of the droplet diameter distribution is significantly improved after the nozzle is charged. Notably, the R.S is small (i.e., 0.610) at 0.1 MPa/0 kV. After adding the electric field, the R.S does not decrease but rather increases to a value between 0.786 and 0.94, while the change trend of voltage does not seem to follow an obvious law. The analysis shows that due to the insufficient atomization capacity of 0.1 MPa gas, the droplet diameter is generally large, so the droplet diameter distribution span is small. Although the atomization ability is improved to some extent after charging, the atomization ability is still limited, and the droplet diameter distribution span only increases slightly. The uniformity of droplet diameter distribution is improved by liquid charging in the effective range of MQL atomization.

6.2 Percentage concentrations of PM10 and PM2.5

Inhalable particles carried by air pose a threat to the environment and the health of operators. Thus, the percentage concentration of PM10 under different working conditions is measured in the experiment (Fig. 20). Under the pure pneumatic atomization condition, the percentage concentration increases significantly with the increase in air pressure. When

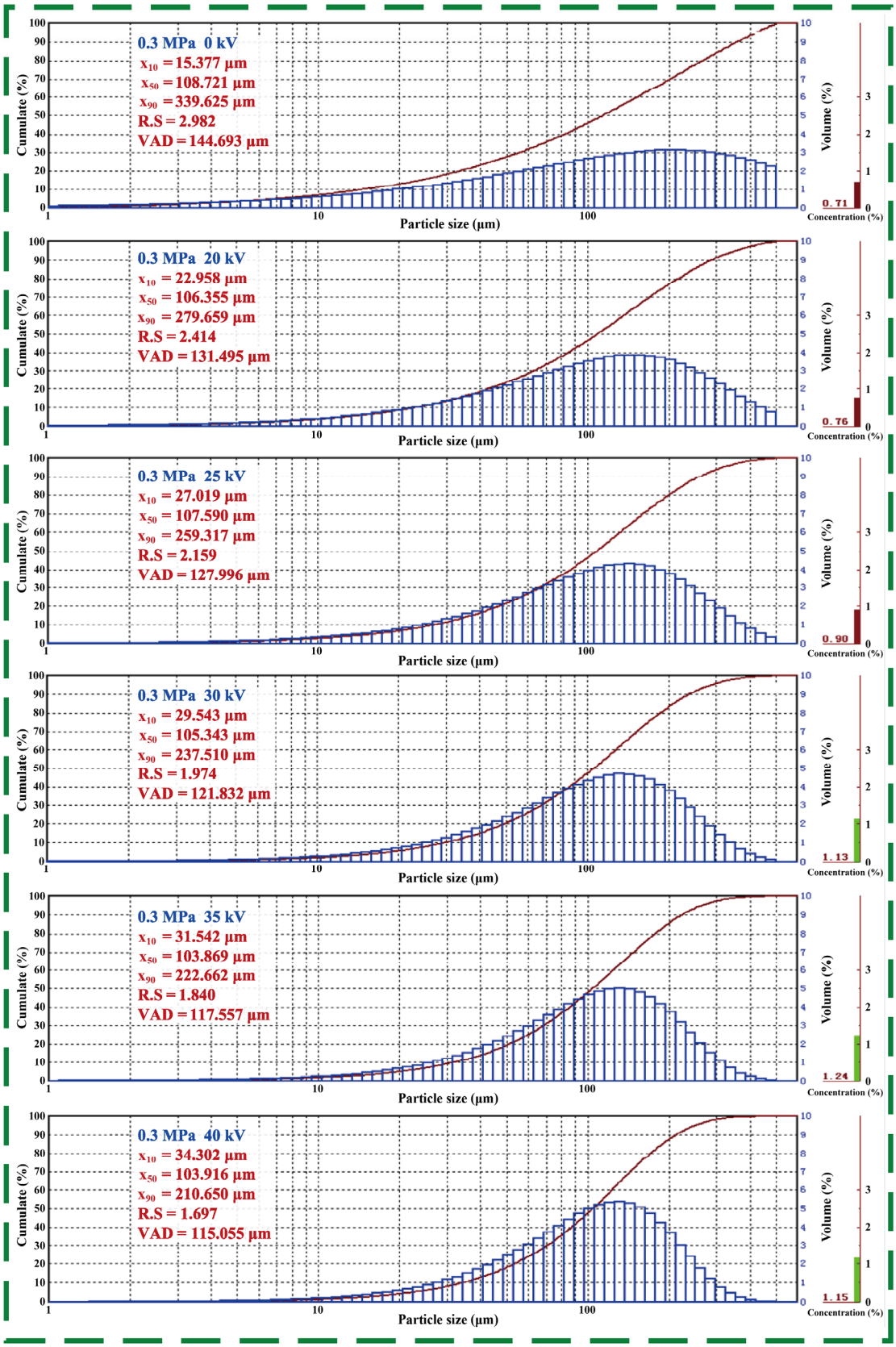

Fig. 18 Measurement of spray particle size under 0.3 MPa condition.

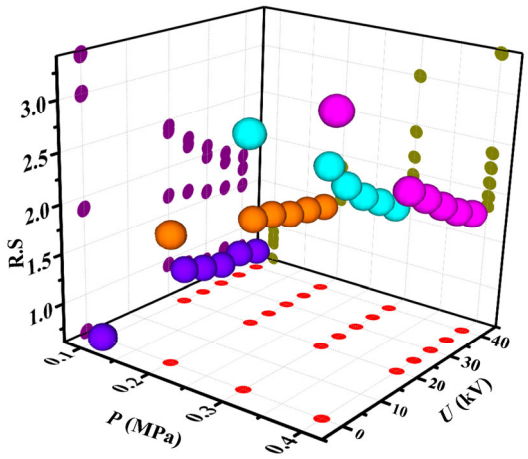

Fig. 19 Spray particle size distribution spans under different working conditions.

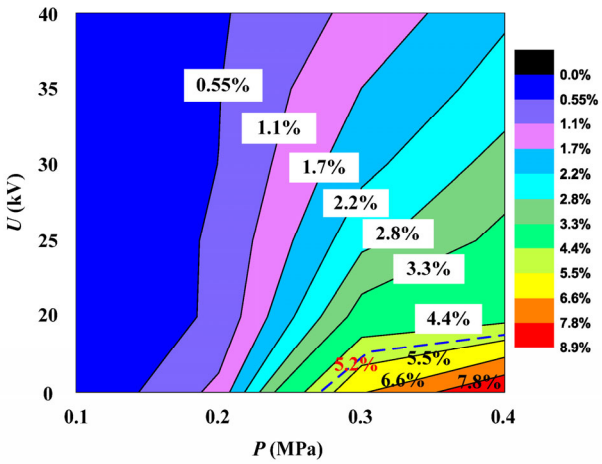

Fig. 20 Percentage concentrations of PM10 under different working conditions.

the air pressure is 0.1–0.4 MPa, the percentage concentrations are 0%, 1.263%, 6.576%, and 8.858%. The analysis shows that when the air pressure is 0.1 MPa, the droplet diameter is greater than 300 μm due to the low atomization energy. No droplet of diameter less than 10 μm is generated. With the increase in gas pressure, the energy exchange between gas and liquid tends to intensify. Furthermore, due to the non-uniformity and superposition of fluctuations of the liquid film, ligaments with an extremely small diameter are formed and broken into fine droplets with very small diameters. With the increase in gas pressure, the probability of producing fine droplets is greater. When the air pressure reaches 0.4 MPa, the percentage concentration of PM10 reaches the maximum at 8.858%. After the nozzle is charged, when the air pressure is 0.1 MPa, the percentage concentration is between 0.001% and 0.003%. The addition of an electric field can improve the atomization ability, allowing for the formation of some fine droplets. As for conditions involving extremely low concentrations, they are no longer analyzed in this research. Under the charged atomization condition, when the air pressure is 0.2–0.4 MPa, the liquid charge has an obvious inhibitory effect on the percentage concentration of PM10. A decreasing trend of percentage concentration is observed with the increase in voltage. The percentage concentrations at 0.2 MPa and 20 and 40 kV are reduced by 48.3% and 61.2%, respectively, compared with that for pure pneumatic atomization at 0.2 MPa. At 0.3 MPa and 20 and 40 kV, the percentage concentrations are reduced by 44.94% and 80.72%, respectively, compared with that for pure pneumatic atomization at 0.3 MPa. The percentage concentrations at 0.4 MPa and 20 and 40 kV are reduced by 54.56% and 76.07%, respectively, compared with that for pure pneumatic atomization at 0.4 MPa. After adding an electric field, the liquid film spreads more evenly, avoiding the formation of extremely thin ligaments caused by the instability of gas drag. The transverse distribution of the liquid film is also more uniform. The comprehensive analysis indicates that the percentage concentration of PM10 can be effectively reduced after the liquid is charged.

In accordance with the third interim target of the World Health Organization and the hygienic standard of inhalable particulate matter in indoor air of China [62], the percentage concentration of PM10 should not be higher than 150 μg/m^3. The flow rate of MQL lubricant in this study is 60 mL/h, and the lubricant density is 916.8 kg/m^3. The average settling time of the PM10 suspended particles is 8.5 s, and the total liquid mass injected at this period is 152.8×10^3 μg. Droplet diffusion space is determined based on equipment and installation space. According to the volume and operation space of ordinary small machine tools, the estimated floor area is 3 m × 3 m, the workshop height is 5 m, and the available diffusion space is 45 m^3. The calculation shows that for PM10 concentration in space to be lower than 150 μg/m^3, the percentage concentration of this particle in the atomized droplets should be less than 5.2%. As shown

in Fig. 20, under the no-charge condition, when the air pressure is between 0.3 and 0.4 MPa, the percentage concentration of PM10 exceeds the hygienic standard of particulate matter. The blue dotted line in Fig. 20 represents the standard line. The area below this standard line does not meet the indoor particle concentration requirements, indicating great harm to the health of operators. Charging the nozzle at 0.1–0.4 MPa allows for the percentage concentration of PM10 to meet the international health standards.

The change trend of percentage concentration of PM2.5 is consistent with that of PM10, as shown in Fig. 21. When the air pressure is 0.1 MPa, the percentage concentration of PM2.5 is not detectable at the nozzle outlet. The percentage concentration increases significantly with the rise in air pressure. Under the pure pneumatic atomization condition at 0.2–0.4 MPa, the percentage concentrations are 0.147%, 1.232%, and 1.748%. According to the analysis, PM2.5-suspended droplets are usually satellite droplets formed during the rapid retraction of ligament rupture. The build-up of satellite droplets is related to the movement speed of the main droplets to a certain extent. The higher the speed of the main droplet, the easier it is to form satellite droplets, and finer droplets are produced. Given the same air pressure condition, the charge has an obvious inhibitory effect on the percentage concentration of PM2.5. In particular, the percentage concentration shows a decreasing trend with the increase in voltage. The percentage concentrations of PM2.5 at 0.2 MPa and 20 and 40 kV are reduced by 64.63% and 80.27%, respectively, compared with that for pure pneumatic atomization at 0.2 MPa. The percentage concentrations at 0.3 MPa and 20 and 40 kV are reduced by 60.31% and 92.05%, respectively, compared with that for pure pneumatic atomization at 0.3 MPa. The percentage concentrations at 0.4 MPa and 20 and 40 kV are reduced by 69.97% and 89.24%, respectively, compared with that for pure pneumatic atomization at 0.4 MPa. The analysis shows that after adding an electric field, the liquid surface tension decreases, which reduces the retraction speed of the ligament fracture and even the possibility of production of satellite droplets. Figure 8 illustrates the formation of a relatively straight ligament after charging, whereas it is bent under the pure pneumatic atomization condition. Therefore, charging can prevent the main droplets from moving directly against the wind to a certain extent, thereafter avoiding the formation of a large number of satellite droplets. National Health Commission of the People's Republic of China have not specified provisions regarding PM2.5 concentrations in the hygienic standards for inhalable particulate matter in indoor air. According to Ref. [63], PM2.5 particles are suspended in air for a much longer time, indicating prolonged periods of harm to the human body and the environment. Accordingly, PM2.5 concentrations should be minimized as much as possible in manufacturing work settings. Figure 21 shows a significant decrease in the percentage concentration of PM2.5 produced by the atomization system after charging. When the air pressure is 0.4 MPa, the percentage concentrations are reduced by 66.67% to 90% compared with that under the no-charge condition. In summary, electrostatic atomization can not only refine the droplet diameter but also reduce the droplet diameter distribution span and the percentage concentrations of PM2.5 and PM10.

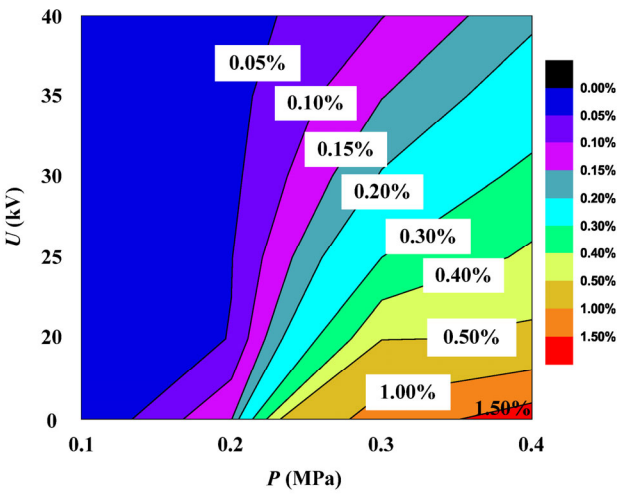

Fig. 21 Percentage concentrations of PM2.5 under different working conditions.

7 Conclusions

This study has collected the fluctuation information of liquid film at the nozzle outlet (i.e., internally mixed two-phase flow nozzle) under different working conditions by using a high-speed camera

system. The effects of air pressure and voltage on the transverse fluctuation of the liquid film, the diameter of the liquid line, and the longitudinal fluctuation of the liquid film are analyzed. The mathematical model of the breaking mechanism of the annular liquid film wave is established, and the accuracy of the model is analyzed. The R.S of droplet diameter distribution span and the percentage concentrations of PM10/PM2.5 under different working conditions are measured by the laser particle sizer (Winner319), and then compared.

1) The formation and unstable breaking mechanism of the annular liquid film in the internal mixing two-phase flow nozzle are analyzed. The instability and fragmentation process of the annular liquid film under different air pressure and voltage conditions are observed by high-speed micrography (PIV). Compared with the findings for the working condition of pure pneumatic atomization, an obvious Taylor cone structure develops at the nozzle outlet under the working condition of electrostatic atomization, the number of transverse wave peaks increases, and the distribution of wave peaks is more uniform. The higher the voltage, the more obvious the abovementioned phenomenon. In addition, with the increase in voltage, the speed of ligament breakup increases, and the breaking length of the ligament decreases.

2) The relationship between true charge mass ratio and change in surface tension is obtained by calculating the limit charge mass ratio of static droplets. The theoretical model of the liquid film's transverse and longitudinal wavelengths in gas-assisted electrostatic atomization is constructed based on the wave instability theory. As for the liquid crushing process, the droplet VAD model, which is positively related to the thickness, transverse wavelength, and longitudinal half-wavelength of the liquid film, is constructed according to the principle of constant volume.

3) The VADs of the droplets under different working conditions are measured using the laser particle sizer, and then compared with the results of the mathematical model. According to the comparative results, the error of the mathematical model in terms of droplet VAD is less than 10%. The model has high accuracy, and thus can be applied.

4) The R.S values of the droplet diameter distribution span and the percentage concentrations of PM10/PM2.5 under different working conditions are compared and analyzed. The results indicate that electrostatic atomization can not only reduce the droplet diameter distribution span but also significantly inhibit the production of PM10 and PM2.5 fine particles. When the air pressure is 0.3 MPa and the voltage is 20 kV and 40 kV, the percentage concentrations of PM10 are reduced by 44.94% and 80.72%, respectively, compared with that under the pure pneumatic atomization condition. As for the percentage concentrations of PM2.5, they are correspondingly reduced by 60.31% and 92.05%.

In conclusion, charging not only increases the atomization performance of soybean oil, but also effectively inhibits the generation of inhalable oil mist particles.

Acknowledgements

This research was financially supported by the National Natural Science Foundation of China (Grant Nos. 52105457 and 51975305), the National Key R&D Program of China (Grant No. 2020YFB2010500), Major Science and Technology Innovation Engineering Projects of Shandong Province (Grant No. 2019JZZY020111), and General project of Liaoning Provincial Department of Education (Grant No. LJKMZ20220971).

Declaration of competing interest

The authors have no competing interests to declare that are relevant to the content of this article.

References

[1] Tang L Z, Zhang Y B, Li C H, Zhou Z M, Nie X L, Chen Y, Cao H J, Liu B, Zhang N Q, Said Z, et al. Biological stability of water-based cutting fluids: Progress and application. *Chin J Mech Eng* **35**(1): 3 (2022)

[2] Duan Z J, Li C H, Zhang Y B, Dong L, Bai X F, Yang M, Jia D Z, Li R Z, Cao H J, Xu X F. Milling surface roughness for 7050 aluminum alloy cavity influenced by nozzle position of nanofluid minimum quantity lubrication. *Chin J Aeronaut* **34**(6): 33–53 (2021)

[3] Ni J, Feng K, He L H, Liu X F, Meng Z. Assessment of water-based cutting fluids with green additives in broaching. *Friction* **8**(6): 1051–1062 (2020)

[4] Liu M Z, Li C H, Zhang Y B, An Q L, Yang M, Gao T, Mao C, Liu B, Cao H J, Xu X F, et al. Cryogenic minimum quantity lubrication machining: From mechanism to application. *Front Mech Eng* **16**(4): 649–697 (2021)

[5] Gupta M K, Sood P K. Surface roughness measurements in NFMQL assisted turning of titanium alloys: An optimization approach. *Friction* **5**(2): 155–170 (2017)

[6] Yang M, Li C H, Luo L, Li R Z, Long Y Z. Predictive model of convective heat transfer coefficient in bone micro-grinding using nanofluid aerosol cooling. *Int Commun Heat Mass* **125**: 105317 (2021)

[7] Sharma A K, Katiyar J K, Bhaumik S, Roy S. Influence of alumina/MWCNT hybrid nanoparticle additives on tribological properties of lubricants in turning operations. *Friction* **7**(2): 153–168 (2019)

[8] Zhang Y B, Li H N, Li C H, Huang C Z, Ali H M, Xu X F, Mao C, Ding W F, Cui X, Yang M, et al. Nano-enhanced biolubricant in sustainable manufacturing: From processability to mechanisms. *Friction* **10**(6): 803–841 (2022)

[9] Gao T, Li C H, Wang Y Q, Liu X S, An Q L, Li H N, Zhang Y B, Cao H J, Liu B, Wang D Z, et al. Carbon fiber reinforced polymer in drilling: From damage mechanisms to suppression. *Compos Struct* **286**: 115232 (2022)

[10] Xu M, Yu X, Ni J. Penetration and lubrication evaluation of vegetable oil with nanographite particles for broaching process. *Friction* **9**(6): 1406–1419 (2021)

[11] Wang X M, Li C H, Zhang Y B, Said Z, Debnath S, Sharma S, Yang M, Gao T. Influence of texture shape and arrangement on nanofluid minimum quantity lubrication turning. *Int J Adv Manuf Tech* **119**(1–2): 631–646 (2022)

[12] Pratap A, Patra K. Combined effects of tool surface texturing, cutting parameters and minimum quantity lubrication (MQL) pressure on micro-grinding of BK7 glass. *J Manuf Process* **54**: 374–392 (2020)

[13] Yang M, Li C H, Said Z, Zhang Y B, Li R Z, Debnath S, Ali H M, Gao T, Long Y Z. Semiempirical heat flux model of hard-brittle bone material in ductile microgrinding. *J Manuf Process* **71**: 501–514 (2021)

[14] Zhang Z C, Sui M H, Li C H, Zhou Z M, Liu B, Chen Y, Said Z, Debnath S, Sharma S. Residual stress of grinding cemented carbide using MoS_2 nano-lubricant. *Int J Adv Manuf Tech* **119**(9): 5671–5685 (2022)

[15] Duan Z J, Li C H, Zhang Y B, Yang M, Gao T, Liu X, Li R Z, Said Z, Debnath S, Sharma S. Mechanical behavior and semiempirical force model of aerospace aluminum alloy milling using nano biological lubricant. *Front Mech Eng* **18**(1): 4 (2023)

[16] Cui X, Li C H, Zhang Y B, Ding W F, An Q L, Liu B, Li H N, Said Z, Sharma S, Li R Z, et al. Comparative assessment of force, temperature, and wheel wear in sustainable grinding aerospace alloy using biolubricant. *Front Mech Eng* **18**(1): 3 (2023)

[17] Yang Y Y, Yang M, Li C H, Li R Z, Said Z, Ali H M, Sharma S. Machinability of ultrasonic vibration assisted micro-grinding in biological bone using nanolubricant. *Front Mech Eng* **18**(1): 1 (2023)

[18] Inamura T, Katagata N, Nishikawa H, Okabe T, Fumoto K. Effects of prefilmer edge thickness on spray characteristics in prefilming airblast atomization. *Int J Multiphas Flow* **121**: 103117 (2019)

[19] Brend M A, Barker A G, Carrotte J F. Measurements of fuel thickness for prefilming atomisers at elevated pressure. *Int J Multiphas Flow* **131**: 103313 (2020)

[20] Shanmugadas K P, Manuprasad E S, Chiranthan R N, Chakravarthy S R. Fuel placement and atomization inside a gas-turbine fuel injector at realistic operating conditions. *P Combust Inst* **38**(2): 3261–3268 (2021)

[21] Chaussonnet G, Gepperth S, Holz S, Koch R, Bauer H J. Influence of the ambient pressure on the liquid accumulation and on the primary spray in prefilming airblast atomization. *Int J Multiphas Flow* **125**: 103229 (2020)

[22] Qin L Z, Yi R, Yang L J. Theoretical breakup model in the planar liquid sheets exposed to high-speed gas and droplet size prediction. *Int J Multiphas Flow* **98**: 158–167 (2018)

[23] Schillaci E, Antepara O, Balcázar N, Serrano J R, Oliva A. A numerical study of liquid atomization regimes by means of conservative level-set simulations. *Comput Fluids* **179**: 137–149 (2019)

[24] Déjean B, Berthoumieu P, Gajan P. Experimental study on the influence of liquid and air boundary conditions on a planar air-blasted liquid sheet, Part I: Liquid and air thicknesses. *Int J Multiphas Flow* **79**: 202–213 (2016)

[25] Lilan H Q, Qian J B, Pan N. Study on atomization particle size characteristics of two-phase flow nozzle. *J Intell Fuzzy Syst* **40**(4): 7837–7847 (2021)

[26] Pillai A L, Nagao J, Awane R, Kurose R. Influences of liquid fuel atomization and flow rate fluctuations on spray combustion instabilities in a backward-facing step combustor. *Combust Flame* **220**: 337–356 (2020)

[27] Zhang Y, Yu N J, Tian H, Li W D, Feng H. Experimental and numerical investigations on flow field characteristics of pintle injector. *Aerosp Sci Technol* **103**: 105924 (2020)

[28] Dafsari R A, Lee H J, Han J, Lee J. Evaluation of the atomization characteristics of aviation fuels with different viscosities using a pressure swirl atomizer. *Int J Heat Mass Tran* **145**: 118704 (2019)

[29] Bravo L, Kim D, Ham F, Powell C, Kastengren A. Effects of fuel viscosity on the primary breakup dynamics of a high-speed liquid jet with comparison to X-ray radiography. *P Combust Inst* **37**(3): 3245–3253 (2019)

[30] Gupta K, Laubscher R F, Davim J P, Jain N K. Recent developments in sustainable manufacturing of gears: A review. *J Clean Prod* **112**(4): 3320–3330 (2016)

[31] Lv T, Xu X F, Yu A B, Niu C C, Hu X D. Ambient air quantity and cutting performances of water-based Fe_3O_4 nanofluid in magnetic minimum quantity lubrication. *Int J Adv Manuf Tech* **115**(5): 1711–1722 (2021)

[32] Krolczyk G M, Maruda R W, Krolczyk J B, Wojciechowski S, Mia M, Nieslony P, Budzik G. Ecological trends in machining as a key factor in sustainable production—A review. *J Clean Prod* **218**: 601–615 (2019)

[33] Zhai S R, Albritton D. Airborne particles from cooking oils: Emission test and analysis on chemical and health implications. *Sustain Cities Soc* **52**: 101845 (2020)

[34] Lee T, Gany F. Cooking oil fumes and lung cancer: A review of the literature in the context of the U.S. population. *J Immigr Minor Healt* **15**(3): 646–652 (2013)

[35] Chen B, Gao D R, Li Y B, Chen C Q, Yuan X M, Wang Z S, Sun P. Investigation of the droplet characteristics and size distribution during the collaborative atomization process of a twin-fluid nozzle. *Int J Adv Manuf Tech* **107**(3): 1625–1639 (2020)

[36] Bhise D K, Patil B T, Shaikh V A. Air assisted atomization characterization of biodegradable fluid using microlubrication technique. *Mater Sci Forum* **1019**: 211–217 (2021)

[37] Li C H, Jia D Z, Yang M, Zhang Y B, Dong L, Hou Y L. Micro lubrication grinding system of controlled jet by electrostatic atomization of nanofluids. CN. Patent CN103072084B, Sep. 2015. (in Chinese)

[38] Mishra R R, Bag R, Panda A, Kumar R, Sahoo A K. Effectiveness of multi position, electrostatic and nanofluid based minimum quantity lubrication: A brief review. *Mater Today Proc* **26**(2): 1099–1102 (2020)

[39] Jia D Z, Zhang Y B, Li C H, Yang M, Gao T, Said Z, Sharma S. Lubrication-enhanced mechanisms of titanium alloy grinding using lecithin biolubricant. *Tribol Int* **169**: 107461 (2022)

[40] Jia D Z, Li C H, Zhang Y B, Yang M, Cao H J, Liu B, Zhou Z M. Grinding performance and surface morphology evaluation of titanium alloy using electric traction bio micro lubricant. *J Mech Eng* **58**(5): 198–211 (2022) (in Chinese)

[41] Xu W H, Li C H, Zhang Y B, Ali H M, Sharma S, Li R Z, Yang M, Gao T, Liu M Z, Wang X M, et al. Electrostatic atomization minimum quantity lubrication machining: From mechanism to application. *Int J Extrem Manuf* **4**(4): 042003 (2022)

[42] Huang S Q, Lv T, Wang M H, Xu X F. Effects of machining and oil mist parameters on electrostatic minimum quantity lubrication—EMQL turning process. *Int J Pr Eng Man-GT* **5**(2): 317–326 (2018)

[43] Lv T, Xu X F, Yu A B, Hu X D. Oil mist concentration and machining characteristics of SiO_2 water-based nano-lubricants in electrostatic minimum quantity lubrication—EMQL milling. *J Mater Process Technol* **290**: 116964 (2021)

[44] Shah P, Gadkari A, Sharma A, Shokrani A, Khanna N. Comparison of machining performance under MQL and ultra-high voltage EMQL conditions based on tribological properties. *Tribol Int* **153**: 106595 (2021)

[45] Su Y, Gong L, Cao H, Chen D D. Optimization of electrostatic atomization cutting using 3D FE simulation of electrostatic field. *Key Eng Mater* **693**: 1255–1262 (2016)

[46] De Bartolomeis A, Newman S T, Shokrani A. Initial investigation on surface integrity when machining Inconel 718 with conventional and electrostatic lubrication. *Procedia CIRP* **87**: 65–70 (2020)

[47] Kim J Y, Lee S Y. Dependence of spraying performance on the internal flow pattern in effervescent atomizers. *Atomization Spray* **11**(6): 735–756 (2001)

[48] Cherdantsev A V, Markovich D M. Evolution of views on the wavy structure of a liquid film in annular dispersed

gas–liquid flow. *J Appl Mech Tech Ph* **61**(3): 331–342 (2020)

[49] Guan X Y, Jia B Q, Yang L J, Fu Q F. Linear instability of an annular liquid jet with gas velocity oscillations. *Phys Fluids* **33**(5): 054110 (2021)

[50] Isaenkov S V, Cherdantsev A V, Vozhakov I S, Cherdantsev M V, Arkhipov D G, Markovich D M. Study of primary instability of thick liquid films under strong gas shear. *Int J Multiphas Flow* **111**: 62–81 (2019)

[51] Wang M, Tian B, Sun Y, Zhang Z. Lump, mixed lump–stripe and rogue wave–stripe solutions of a (3+1)-dimensional nonlinear wave equation for a liquid with gas bubbles. *Comput Math Appl* **79**(3): 576–587 (2020)

[52] Zhang Q, Yang F Z, Li C C, Wang X, Cao T T, Li C H, Liu Q. Numerical study on the breakup mechanisms and characteristics of liquid sheets. *Energ Source Part A* https://doi.org/10.1080/15567036.2020.1818891 (2020).

[53] Daskiran C, Xue X Z, Cui F D, Katz J, Boufadel M C. Large eddy simulation and experiment of shear breakup in liquid–liquid jet: Formation of ligaments and droplets. *Int J Heat Fluid Fl* **89**: 108810 (2021)

[54] Vadivukkarasan M, Panchagnula M V. Helical modes in combined Rayleigh–Taylor and Kelvin–Helmholtz instability of a cylindrical interface. *Int J Spray Combust* **8**(4): 219–234 (2016)

[55] Jin X, Shen C B, Lin S, Zhou R. Experimental study on the spray characteristics of a gas–liquid pintle injector element. *J Visual* **25**(3): 467–481 (2022)

[56] Li F, Yin X Y, Yin X Z. Instability analysis of an inner-driving coaxial jet inside a coaxial electrode for the non-equipotential case. *J Electrostat* **66**(1–2): 58–70 (2008)

[57] Grigor'ev A I, Shiryaeva S O. Electrostatic instability of the higher-order azimuthal modes of a charged jet. *Fluid Dynam* **56**(3): 353–360 (2021)

[58] Bang B H, Kim M W, Kim Y I, Yoon S S. Growth rate and oscillation frequency of electrified jet and droplet: Effects of charge and electric field. *Aerosol Sci Tech* **52**(9): 1070–1082 (2018)

[59] Yin P T, Han X S, Bi D, Duan T X, Hu B. Experimental studies on liquid producing plasma of high voltage electrostatic atomization. *Telecom Power Technol* **31**(3): 68–70 (2014) (in Chinese)

[60] Chu W, Li X Q, Tong Y H, Nie W S, Jiang C J, Ren Y J. Numerical study on breakup characteristics of liquid film of liquid-centered swirl coaxial injectors. *Journal of Propulsion Technology* **42**(7): 1522–1533 (2021) (in Chinese)

[61] Shen Q G, Fang Y, Zhou Z C, Wang D Z. *High Voltage Technology*, 4th edn. Beijing (China): China Electric Power Press, 2012. (in Chinese)

[62] CN-GB. GB/T 17095-1997 Hygienic standard for inhalable particulate matter in indoor air. CN-GB, 1997. (in Chinese)

[63] Jia D Z, Zhang N Q, Liu B, Zhou Z M, Wang X P, Zhang Y B, Mao C, Li C H. Particle size distribution characteristics of electrostatic minimum quantity lubrication and grinding surface quality evaluation. *Diam Abrasives Eng* **41**(3): 89–95 (2021) (in Chinese)

Dongzhou JIA. He is a lecturer of Liaoning University of Technology (LNUT), China. He received his Ph.D. degree from Qingdao University of Technology (QUT), China, in 2021. His current research interests focus on intelligent and clean precision manufacturing. He has published 26 papers, including in *Tribology International* and *International Journal of Machine Tools and Manufacture*. Among them, one is Essential Science Indicators (ESI) highly cited papers.

Changhe LI. He is a professor of QUT. He is a special expert of Taishan Scholars in Shandong Province, China. He received his Ph.D. degree from Northeastern University, China, in 2006. His current research interests focus on intelligent and clean precision manufacturing. He has published 153 SCI/EI papers and won the China Patent Excellence Award (2 items) and Shandong Province Technical Invention 1st Prize.

Yanbin ZHANG. He is a professor of QUT. He is a Xiangjiang Scholar from The Hong Kong Polytechnic University. He received his Ph.D. degree from QUT in 2018. His current research interests focus on intelligent and clean precision manufacturing. He has published 35 papers, including in *International Journal of Machine Tools and Manufacture* and *Journal of Materials Processing Technology*. Among them, one is ESI hot paper, and three are ESI highly cited papers.